RSC Advances

PAPER

View Article Online
View Journal | View Issue

Cite this: *RSC Adv.*, 2022, **12**, 27396

Alternating magnetic field and NIR energy conversion on magneto-plasmonic Fe_3O_4@APTES–Ag heterostructures with SERS detection capability and antimicrobial activity

Magdalena Kulpa-Greszta, *[a] Anna Tomaszewska, [a] Anna Michalicha, [b] Daniel Sikora, [a] Andrzej Dziedzic,[c] Renata Wojnarowska-Nowak,[d] Anna Belcarz[b] and Robert Pązik *[a]

Multipurpose Fe_3O_4@APTES–Ag heterostructures for mutual heat generation, SERS probing, and antimicrobial activity were fabricated using a three-step process. Silver metallic particles were precipitated on a thin silica shell that served as an interlayer with Fe_3O_4 nanocubes. The structural properties were studied by means of the powder X-ray diffraction technique, and selected area electron diffraction. Particle size, distribution, and morphology were evaluated using transmission electron microscopy, while element mapping was performed using the STEM-EDS technique. The presence of the silica shell and the effectiveness of the Ag reduction were checked by FTIR-ATR spectroscopy. The heat generation ability was studied by using AMF and NIR contactless external stimulations working separately and simultaneously. We demonstrated that the dual mode stimulation leads to a SAR (specific absorption rate) of 1000 W g^{-1} with the predominant role of the mechanism associated with the light interaction. The SERS effect was recorded with the use of the R6G standard molecule showing high capability of the heterostructures for Raman signal augmentation. Fe_3O_4 nanocubes decorated with Ag particles have shown antibacterial activity against *P. aeruginosa*. The Fe_3O_4@APTES–Ag presents promising potential as a multipurpose platform for biological applications ranging from photomagnetic therapies, to analytical probes exploiting the SERS effect and antibacterial activity.

Received 19th August 2022
Accepted 19th September 2022

DOI: 10.1039/d2ra05207e

rsc.li/rsc-advances

1. Introduction

The ability of magnetite nanoparticles (MNPs, Fe_3O_4) to induce heat under the action of external stimulants is a basis for the biological application of hyperthermia that can support modern therapeutic approaches to cancer treatment.[1] This particular material attribute is directly related to the magnetic properties of Fe_3O_4 and is driven by the general mechanism of power loss that incorporates three main contributions being a consequence to the alternating magnetic field (AMF) exposure.[2] The first one is associated with hysteresis losses that depend on the coercive field and are characteristic of the particles with domain/multidomain structure, the second with generation of eddy currents whose strength is affected by the magnetic field frequency and intensity and their induction changes in the following material classification manner: metals > semiconductors > insulators. The last is connected with the residual losses that can be subdivided into Néel (internal) and Brownian (external) relaxations. Internal relaxation represents fluctuations in MNP magnetic moments, while the external mechanism is due to fluctuations in magnetic moments that cause rotation of the entire particle.[3–7] The presence or absence of one of the power loss mechanisms is strongly dependent on many parameters like particle size, composition, shape, anisotropy, stability, presence of ligands, *etc.*[8]

Laser exposure with wavelengths within the therapeutic optical biological window maximized tissue light penetration (650–1300 nm) is used to heat nanoparticles of different kinds to induce temperature effects.[9] The rule of thumb is to find a highly absorbing material that will dissipate the collected energy non-radiatively (net phonons) to heat a given system to achieve a biologically relevant temperature effect.[10–13] Among many materials exploited, magnetite is a very promising candidate to achieve this goal,[14–18] as its optical properties show reasonable absorption in the near-infrared range (NIR).[19]

[a]*Department of Biotechnology, Institute of Biology and Biotechnology, College of Natural Sciences, University of Rzeszow, Pigonia 1, 35-310 Rzeszow, Poland. E-mail: mkulpa@ur.edu.pl; rpazik@ur.edu.pl*

[b]*Chair and Department of Biochemistry and Biotechnology, Medical University of Lublin, Chodzki 1, 20-093 Lublin, Poland*

[c]*Department of Spectroscopy and Materials, Institute of Physics, College of Natural Sciences, University of Rzeszow, Pigonia 1, 35-310 Rzeszow, Poland*

[d]*Institute of Material Engineering, College of Natural Sciences, University of Rzeszow, Pigonia 1, Rzeszow, Poland*

Recently, considerable interest has been faced towards exploitation of multimodal heat induction by the use of the simultaneous action of AMF and NIR.[20–25] The trick is to take the advantage out of the two totally independent mechanisms of energy conversion into heat that allow to achieve much faster sample heating and reduce the development of thermotolerance by cells that is characteristic of slow heating rates.[26] It is also possible to go beyond the maximum temperature that can be achieved by using separate mode, to limit the concentration of MNPs if needed, or to reduce the overall exposure time. Therefore, the search for new materials with optimized properties and/or offering additional functions is of great importance.

The noble metal decorated magnetite particles, especially with silver and gold, are of special interest since combination of magnetic properties with plasmonic effect have interesting implications. For instance Fe_3O_4@Au heterostructures have been proposed for use as an opto-magnetic platforms,[26] whereas Das *et al.* proposed reversed Ag@Fe_3O_4 composite structures. However, both materials did not show significant enhancement in SAR (specific absorption rate) compared to the commercially available Resovist®. In the case of the Fe_3O_4@Ag decorated hybrid material, not much was done in terms of temperature effects. The main direction was pushed towards surface-enhanced Raman scattering (SERS) for detection of analytes,[27,28] modern and effective catalysts[29–31] or disinfectant with antibacterial activity.[32] The role of the magnetic core in the latter examples was limited to separation agent facilitating collection of the heterostructures from the medium after use with a static magnetic field and particles recycle.

The purpose of the presented studies was to assess the efficiency of energy conversion using combined AMF and NIR (808 nm laser light) external contactless stimulation in the multipurpose heterostructure of Fe_3O_4@APTES–Ag. Except for the significant temperature response of the hybrid material, its multifunctional properties were tested towards the SERS probe for detection of analytes as well as antimicrobial activity was estimated against *Staphylococcus aureus* ATCC 25923, *Staphylococcus epidermidis* ATCC 12228, *Escherichia coli* ATCC 25922 and *Pseudomonas aeruginosa* ATCC 27953 with pronounced effect against the last bacterial strain. Morphology-controlled Fe_3O_4 MNPs (nanocubes) were used as a core material, while (3-aminopropyl)triethoxysilane (APTES) served as an interconnector layer between Fe_3O_4 and Ag, a surface protection agent (prevention of MNP from oxidation and contact with outer media) and as a chelation enhancer due to increased affinity of amine APTES groups for silver cations.

2. Materials and methods

2.1. Three-step synthesis of MNPs core–shell structures decorated with Ag nanoparticles

The synthetic protocol for the fabrication of Fe_3O_4@APTES–Ag core–shell structures included three distinct steps, namely (I) preparation of the Fe_3O_4 nanocubes stock particles, (II) surface coverage of the stock MNPs with the APTES shell, and (III) reduction of silver cations to induce precipitation of metallic Ag nanoparticles.

2.1.1 Synthesis of Fe_3O_4 nanocubes. The stock Fe_3O_4 nanocubes were prepared by adopting the well-known thermal decomposition technique described by Kim *et al.*[33] with slight amendments. Briefly, 2 mmol of iron(III) acetylacetonate precursor ($Fe(acac)_3$; 99.7%, Thermo Fischer Scientific, Germany), 4 mmol (1.4 ml) of oleic acid (OA, 90%, Sigma Aldrich, Poland) and 10 ml of diyl ether (BE, 98%, Sigma Aldrich, Poland) were taken. The iron source was transferred to the three-neck glass flask and dissolved in BE solvent with the subsequent addition of the OA ligand under an inert N_2 protective atmosphere (N_2 99.999%, Linde, Poland) using an acrylic glove box (GS Glove Box Systemtechnik GMBH P10R250T2) with pressure gas control. The flask with mixed chemicals was attached to the setup combined with a mechanical stirrer, automatic temperature controller with Pt-100 sensor (LTR 2500, Juchheim, Germany), reflux column, laboratory heater, and N_2 line. Afterward, the reaction mixture was degassed for one hour at room temperature with a constant flow of N_2. Finally, the solution was heated up to 285 °C and kept for 30 minutes. The resulting black product was separated from the mother liquor by centrifugation and washing cycles using portions of the solvent mixture hexane/acetone/ethanol (1 : 1 : 1 ratio, all pure for analysis from Chempur, Poland). The purified stock nanoparticle suspension is stored in an ethanol solution in a laboratory refrigerator. The concentration of Fe_3O_4 cubes was measured using the microbalance.

2.1.2 APTES silica shell formation. This step involved the following actions. First, 50 mg of well-dispersed Fe_3O_4 nanocubes are transferred to hexane and washed three times with this solvent to completely remove ethanol. If fresh particles are prepared from step (I), the MNPs can be kept directly in hexane after purification. A laboratory magnet can be used to facilitate cube separation if necessary. Finally, Fe_3O_4 particles are resuspended in 5 ml of hexane and sonicated for 2 hours at room temperature. The suspension is transferred to the flask and filled with an additional portion of hexane to 45 ml. After that, 2 ml of IGEPAL CO-520 (polyoxyethylene (5) nonylphenylether, Sigma Aldrich, Poland) was sonicated for an additional 15 minutes. Then, 0.4 ml of ammonia (25% solution, 99%, Honeywell, Poland) was kept in an ultrasound bath for an additional 15 minutes at room temperature. Subsequently, the mixture was placed in a glass flask in the set-up equipped with a mechanical stirrer and 100 μl of tetraethoxysilane (TEOS, 99.9%, Thermo Scientific, Poland) was added in constant mixing for one hour. Lastly, a mixture of 100 μl of TEOS and 100 μl of APTES ((3-aminopropyl)triethoxysilane, 99%, Sigma Aldrich, Poland) was added and left for 16 hours with stirring. The Fe_3O_4@APTES core–shell structures were separated using a laboratory magnet followed by washing cycles with an acetone and ethanol mixture. The concentration of particles was measured using the same technique as in the first step.

2.1.3 Fabrication of metallic Ag nanoparticles on Fe_3O_4@APTES surface. To induce Ag nanoparticle formation, 2 mg Fe_3O_4@APTES were dispersed in 20 ml of deionized water and sonicated for 15 minutes. Subsequently, four portions of 0.1 ml

of $AgNO_3$ solution (99%, POCH, Poland) (1 mg ml^{-1}) were added every 15 minutes. The sample was still placed in an ultrasonic bath during this stage. The entire suspension was then transferred to the glass flask and 0.76 ml of $NaBH_4$ solution (1 mg ml^{-1}, 99% Thermo Scientific, Poland) was added to induce a fast reduction of Ag^+ and the formation of Ag metallic particles under mechanical stirring. The final Fe_3O_4@APTES–Ag product was purified separately with H_2O and ethanol (3 times each solution) and separated with a laboratory magnet. The core–shell material was resuspended in ethanol for storage and further use.

2.2. Characterization of nanoparticle physicochemical properties

Stock Fe_3O_4 nanoparticle structure was evaluated by means of the X-ray powder diffraction technique (XRD) using a Bruker D8 Advance diffractometer equipped with a Cu lamp as the X-ray source (1.54 Å) and $K_{\alpha 2}$ nickel filter. The range of measured 2θ was between 15 and 70° with a step of 0.02° applying 0.8 s integration time. The recorded diffraction pattern was background corrected using Diffrac.Eva software (V.2) and compared with the ICDD diffraction database for structure identification and crystallographic plane assignment. Further data curation (including normalization and reference comparison) for the final presentation was performed using Origin Pro 2019 9.60 software (OriginLab, USA).

The particle size, morphology, additional structural data, and element mapping were performed using Tecnai Osiris X-FEG transmission electron microscope (TEM) operating at 200 kV using different techniques high-resolution TEM (HRTEM), high-angle annular dark-field (HAADF) imaging in scanning transmission electron microscopy (STEM) as well as energy dispersive analysis for confirmation of the presence of silica shell as well as the location of silver particles. Fourier transformation was applied to the HRTEM picture to measure the interplanar distance and identification of exposed crystallographic planes by Fe_3O_4 particles using DigitalMicrograph (v. 1.85.1535) software. The nanocube, silver particle size, and distribution together with silica shell thickness were evaluated in ImageJ software (v. 1.8.0_1720). The sample for TEM characterization was prepared by sonication cycles and further deposition of a droplet of MNPs ethanol suspension on a 200 mesh copper grid coated with a transparent layer of carbon (EM Resolutions, United Kingdom) and slow solvent overnight evaporation under dust protection.

The nanoparticle concentration was determined using the microbalance technique using a precise Radwag MYA 5.4Y scale. The measurement was made through three independent repetitions.

Fourier-transform infrared spectroscopy (FTIR) was used to carry out the measurements of the vibrational spectra of prepared materials utilizing a Thermo Scientific Nicolet iZ10 FTIR spectrometer equipped with Smart Orbit Diamond ATR (attenuated total reflection accessory). All materials were slowly dried and placed on a diamond surface. Spectra were recorded at room temperature within the 4000–500 cm^{-1} wavenumber range.

2.3. AMF and NIR energy conversion on heterostructures

The behavior of the stock nanocubes and Fe_3O_4@APTES–Ag core–shell structures upon the action of the alternating magnetic field (AMF), near-infrared 808 nm laser radiation (NIR), and synergy of both external stimulants was measured with help of magnetic field generator G2 D5 Series Multimode 1500 W driver supplied by Nanoscale Biomagnetics (Spain) using calorimetric CAL1 coilset. The NIR radiation was delivered through 400 μm multimode optical fiber (CNI China). FLIR T660 Thermovision camera was used for a direct measure of sample temperature. The applied field frequency and intensity were within a range of 145–486 kHz and 23–33 kA m^{-1} while laser power was between 0.3–1.7 W. The distance of the optical fiber from the suspension surface was 4 cm assured full top sample coverage (around 1 cm^2). During the synergy of both contactless stimulants, optimized parameters were used (302 kHz, 28 kA m^{-1}, 900 mW). Before experiments, CAL1 was calibrated using manufacturer procedure whereas laser output power was checked using Ophir StarLite power meter with beam track thermal sensor 10A-PPS (Ophir, Israel). All data were recorded using ResearchIR software (FLIR, USA) and analyzed using Origin Pro software. The concentration of the prepared stock suspensions of Fe_3O_4 and Fe_3O_4@APTES–Ag core–shell structures used for energy conversion studies varied between 1–6 mg ml^{-1}.

2.4. Surface-enhanced Raman scattering (SERS) on heterostructures

The ability to generate the SERS effect was analyzed using an inVia Micro Raman Renishaw spectrometer combined with a Leica DM 2500M microscope (Renishaw, UK) equipped with a 488 nm laser as an excitation source. The measurements were taken with an exposure time of 10 s with triple scan accumulation and for the laser output power that ranged from 25 μW to 0.5 mW. As a reference material for testing, rhodamine 6G (R6G, Sigma-Aldrich, Poland) was chosen. Various ethanol dilutions of rhodamine were prepared (0.05–2.5 μM) and mixed with 0.75 mg ml^{-1} of Fe_3O_4 nanocubes, Fe_3O_4@APTES and Fe_3O_4@APTES–Ag heterostructures, respectively. After a short incubation, samples were placed on quartz discs and slowly dried. The final SERS measurement was carried out with a 50× lens magnification and choosing three random positions for each material. Baseline correction was performed during data processing.

2.5. Antimicrobial activity tests with bacteria strains

Antibacterial activity of nanoparticles was evaluated by determination of minimum inhibitory concentration (MIC), on basis of the serial dilution method. As model bacteria, 4 reference strains were used: *Staphylococcus aureus* ATCC 25923, *Staphylococcus epidermidis* ATCC 12228, *Escherichia coli* ATCC 25922, and *Pseudomonas aeruginosa* ATCC 27953. Before the experiments, they were first cultured in Mueller–Hinton (M–H) broth (Biomaxima, Poland) at 37 °C to obtain inoculates of initial density equal to 0.1 McFarland (an equivalent of 3.0×10^7 CFU

ml^{-1}). Suspension of each nanoparticle in ethanol was diluted in Mueller–Hinton (M–H) broth to obtain a series of concentrations: 50–500 μg ml^{-1} for Fe_3O_4 nanoparticles and 1.56–50 μg ml^{-1} for Fe_3O_4@APTES and Fe_3O_4@APTES–Ag core–shell nanoparticles. As reference samples, ethanol was diluted in M–H broth to obtain analogous concentrations as in NPs dilutions. As a positive control of bacterial growth, pure M–H broth was used (separately for each bacterial strain). 200 μl of each NPs suspension, in quadruplicate, was pipetted into wells of a 96-well plate and supplemented with 4 μl of bacterial inoculate (to initial titer 0.6×10^6 CFU ml^{-1}). Pure M–H broth without inoculation was used to control the initial medium sterility. Immediately after the inoculation (T 0 h), the absorbance of the wells was measured at 660 nm in Biotec Synergy H4 Hybrid multiplate reader (Fisher Scientific, USA). Then, the plates were incubated in Innova 42 incubator shaker (New Brunswick Scientific, USA) at 37 °C, 150 rpm, and 24 h. Finally, the turbidity in the wells was examined. MIC (minimum inhibitory concentration) was defined as the lowest concentration of NPs which prevented bacterial growth in the culture medium which was visualized by lack of turbidity in the wells.

3. Results and discussion

3.1. Physicochemical characterization of materials

The structural properties of the core material, namely Fe_3O_4 nanocubes, were evaluated using the XRD technique. The recorded diffraction pattern after background correction and normalization is presented in Fig. 1, and compared with the reference ICDD card (International Centre for Diffraction Data – PDF database) no. 019-0629 that is ascribed to the cubic $Fd\bar{3}m$ magnetite structure. All the appearing reflections, within the measured 2θ range, were assigned to the respective crystallographic planes showing a perfect match with the chosen standard card. In addition, selective area electron diffraction (SAED) was performed on a single particle together with identification of the exposed crystallographic fringes using Fourier transformation applied to the HRTEM image (Fig. 1 right panel). Both measurements confirmed that the stock material crystallized in a cubic symmetry that is characteristic of the ferrite family. The measured interplanar distance of the 0.149 nm (4 4 0) plane agrees with the reference data.

The size, distribution, and morphology of the Fe_3O_4 nanocubes, Fe_3O_4@APTES–Ag, and Ag particles in the core–shell structures were defined using TEM imaging (Fig. 2). Non-modified Fe_3O_4 particles have a predominant cubic morphology that is maintained during the APTES coverage and the Ag^+ reduction step. The particle size and distribution for the stock cubes was 72 ± 13.9 nm, while Fe_3O_4@APTES–Ag was 94.7 ± 15.5 nm, and the Ag nanoparticles were 8.5 ± 3.7 nm. The shape of the Ag precipitate on the surface of Fe_3O_4@APTES is not well defined, and the particles tend to have a rather irregular morphology. In the case of silica modification using APTES, the thickness of the shell was measured giving the mean value of 12.8 ± 3.4 nm. As can be seen, the shell formed by the silica interlayer containing amine functional groups is rather thin. The choice of APTES as a shell-forming material was dictated by the fact that $-NH_2$ functional groups bond Ag^+ cations through chelation, not through sorption as –OH functionality, and ensures a higher affinity towards silver cations.[34] All results have been collected and plotted in Fig. 3 for quick comparison. Interestingly, the particles tend to organize in chain-like structures.

According to Qiao *et al.*,[35] this behavior is characteristic of magnetic particles, where magnetic dipolar interactions between particles dominate (long-range) over van der Waals forces (short range). Usually, this kind of assemblies are observed for magnetite with a size greater than 40 nm. What can be potentially worth mentioning is that this type of self-organization is less pronounced for the Fe_3O_4@APTES–Ag

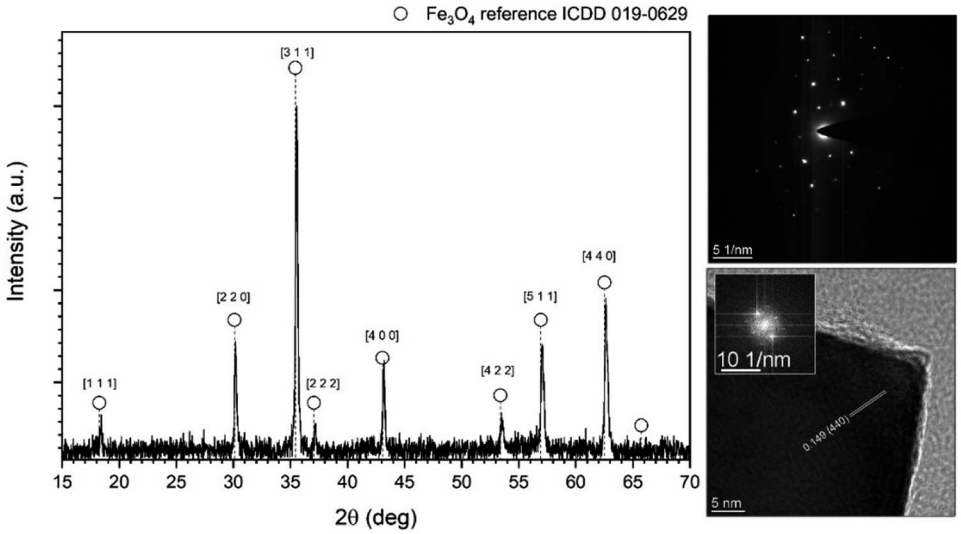

Fig. 1 Indexed X-ray diffraction pattern as well as SAED image with FFT transformation of HRTEM for identification of exposed crystallographic plane of the stock Fe_3O_4 nanocubes.

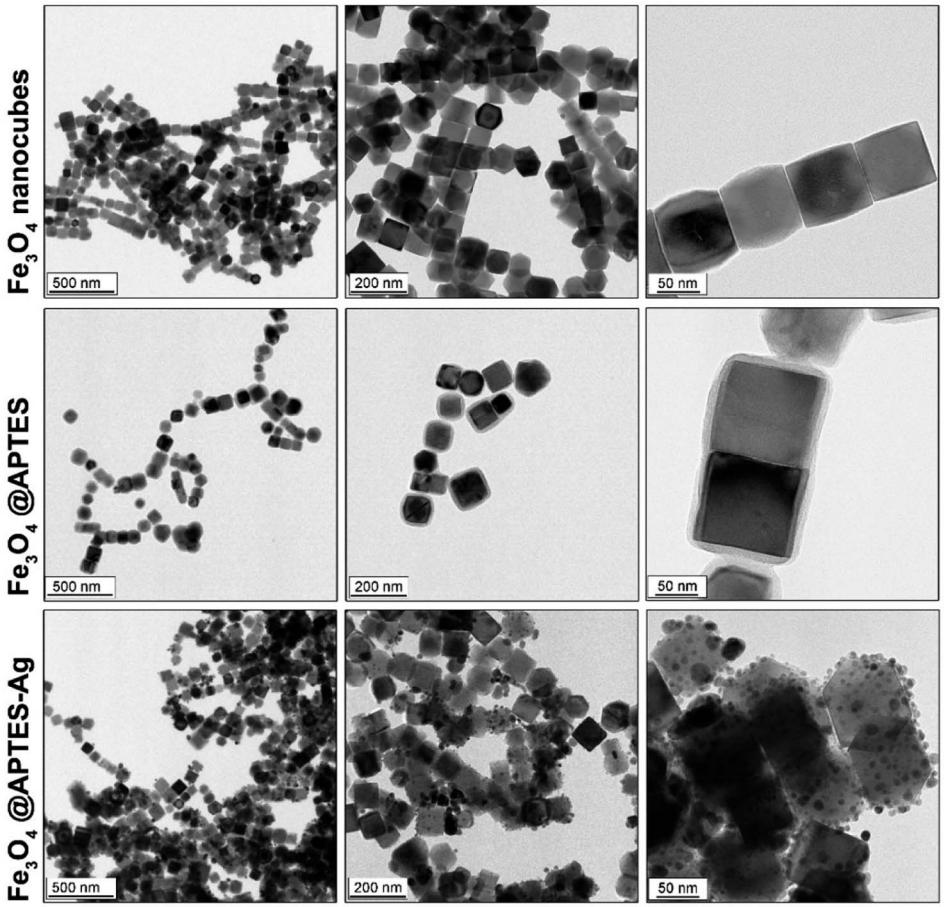

Fig. 2 TEM images of the Fe_3O_4 stock nanocubes, nanocubes covered with a thin shell of APTES as well as Fe_3O_4 decorated Ag metallic nanoparticles on APTES shell.

core–shell since the thickness of the silica shell and Ag size probably reduce the possibility of effective magnetic interactions due that their diameters account for the separation of the magnetic cores between each other.

Element mapping was performed (Fig. 4) using the STEM-HAADF-EDS technique to check the effect of the surface coverage of APTES and silver reduction in terms of the presence of silicon and silver elements in the Fe_3O_4@APTES and

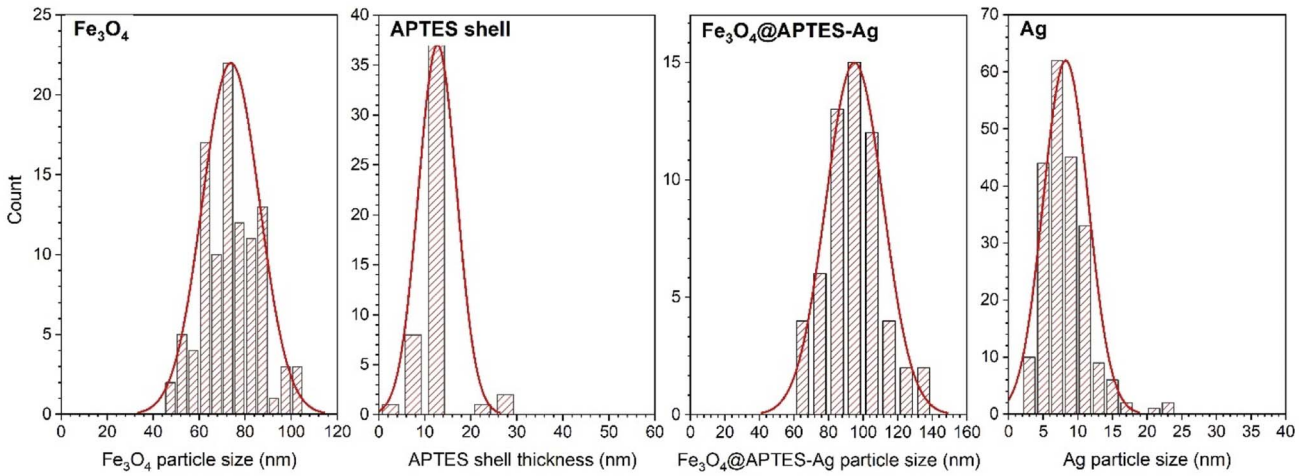

Fig. 3 Particle size distribution curves for Fe_3O_4 stock cubes, APTES shell thickness, Fe_3O_4@APTES–Ag core–shell structures, and Ag particles.

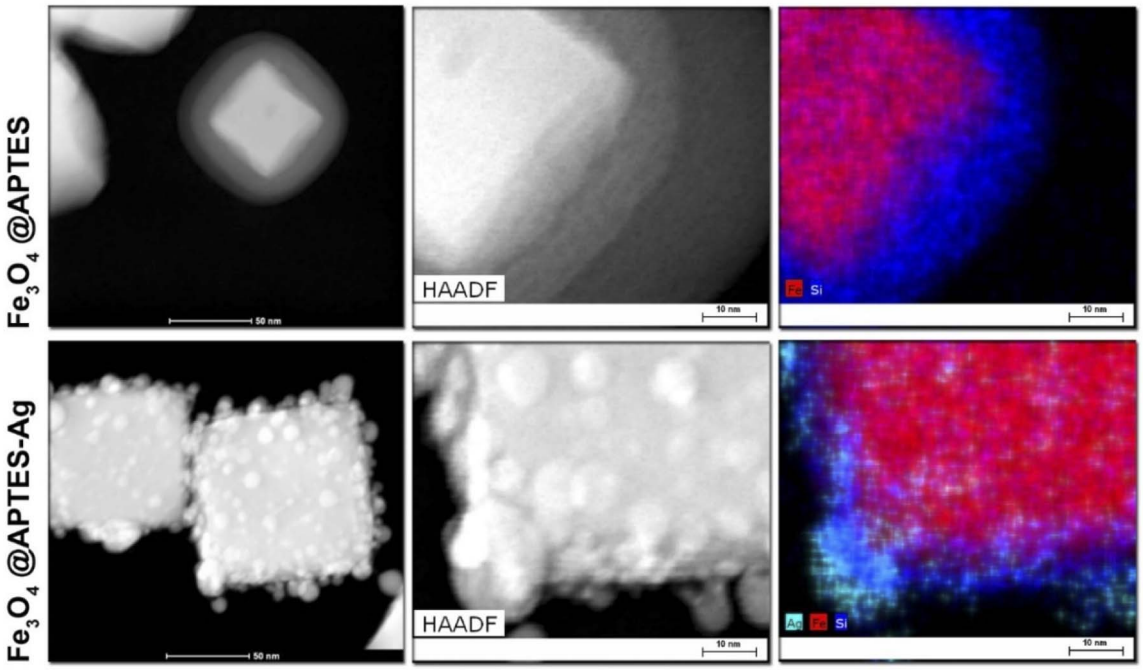

Fig. 4 STEM-HAADF-EDS element mapping of the effect of Fe_3O_4 nanocubes surface modification with APTES and result of the reduction process leading to the formation of the Ag metallic islands.

Fe_3O_4@APTES–Ag structures. It can be seen that the Fe_3O_4 nanocubes were covered with a rather uniform and thin APTES shell. The reduction of adsorbed Ag^+ cations leads to the formation of separated islands of metallic silver, as confirmed by the overlap areas between the Ag element map and the HAADF image that are characteristic of the presence of individual Ag particles bounded to the Fe_3O_4 cubes through the APTES interlayer.

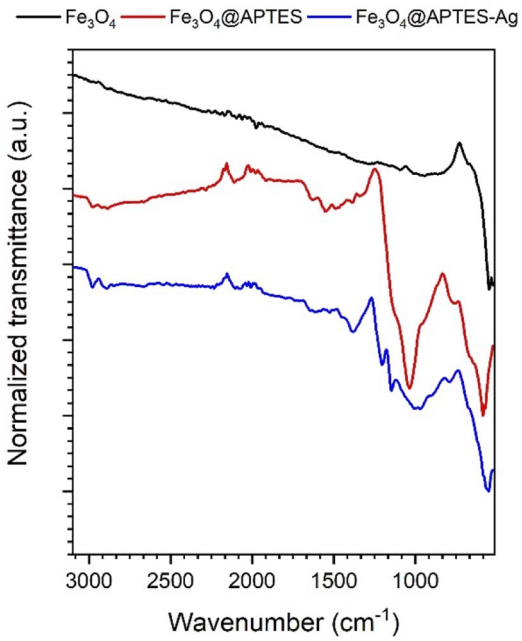

Fig. 5 FTIR-ATR spectra of the stock Fe_3O_4 nanocubes, Fe_3O_4@APTES core–shell and Fe_3O_4@APTES–Ag heterostructures.

The FTIR-ATR spectroscopy was used to record vibrational spectra of Fe_3O_4 nanocubes, Fe_3O_4@APTES core–shell and Fe_3O_4@APTES–Ag heterostructures (see Fig. 5) and to assess the effect of silica surface coverage and silver attachment after the reduction process. The appearance of the Fe_3O_4 nanocubes IR spectra is characteristic of magnetite and consists of the band with a maximum intensity of around 550 cm^{-1} that is generally ascribed to the Fe–O bond vibrations.[36] The Fe_3O_4@APTES shows characteristic bands that are associated with the Si–O–Si modes at 1037, 763 cm^{-1}, Si–OH at 948 cm^{-1}, band at 1635 cm^{-1} associated with NH_2 groups and 1542 cm^{-1} mode of N–H, vibrations of C–H at 2979 and 2892 cm^{-1}, structural units $-CH_2$ and $-CH_3$ at 1488 and 1384 cm^{-1} that give evidence of Fe_3O_4 surface coverage with APTES.[37] In the case of the Fe_3O_4@APTES–Ag the attachment of the metallic particles after reduction is clear since most notable peaks are shifted toward lower energies, especially the ones associated with silica vibration modes.

3.2. AMF and NIR external contactless energy conversion on Fe_3O_4@APTES–Ag structures

Temperature generation was studied using three different modes of stimulation (1) alternating magnetic field followed by optimization of magnetic field frequency and intensity (145–486 kHz, 22–28 kA m^{-1}); (2) 808 nm NIR laser by applying a different output laser power; and (3) under the simultaneous action of both AMF and NIR (dual-mode) performed as a function of

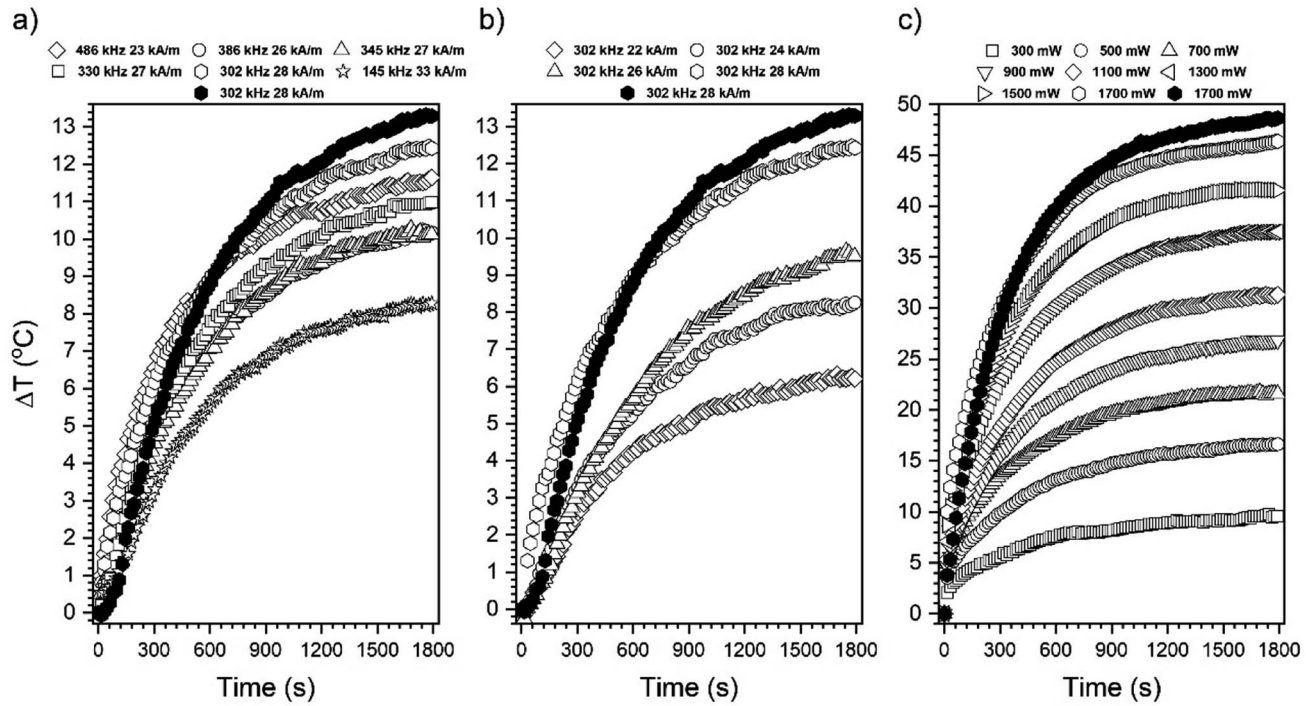

Fig. 6 Heating curves of the Fe_3O_4@APTES–Ag under stimulation with (a) alternating magnetic field, (b) different field intensities for 302 kHz, and (c) 808 nm infrared laser radiation as a function of laser power. The solid black line represents reference Fe_3O_4 nanocubes behavior. The working particle concentration in each case was 1 mg ml^{-1}.

nanoparticle concentration (1–6 mg ml^{-1}) for altering heating effects. The choice of the 808 nm wavelength was motivated by the well-known spectral characteristic of Fe_3O_4 particles and its minimized absorption by water molecules and biological systems.[9,15] Approaches (1) and (2) were used mainly to optimize both stimulant parameters and were carried out on colloids

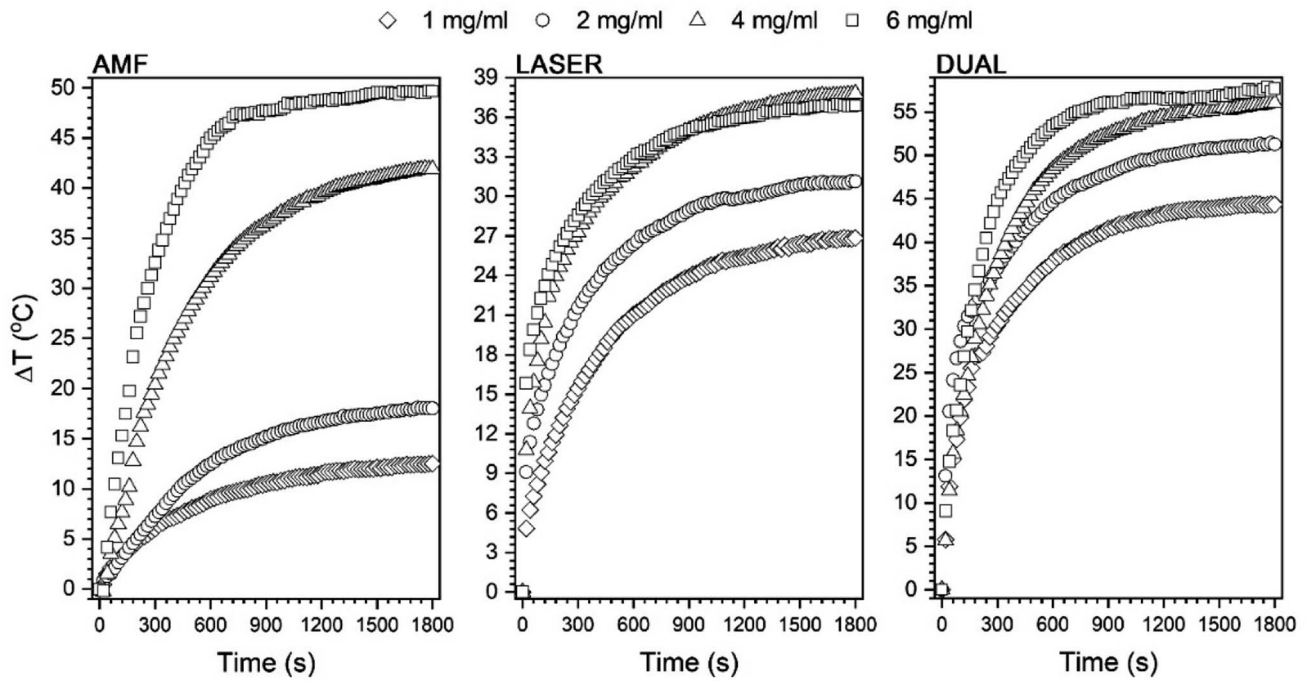

Fig. 7 Concentration dependence of the induced heating effects on Fe_3O_4@APTES–Ag core–shell structures using different modes of external contactless stimulation. DUAL mode represents the simultaneous action of AMF and laser for optimized magnetic field and laser parameters.

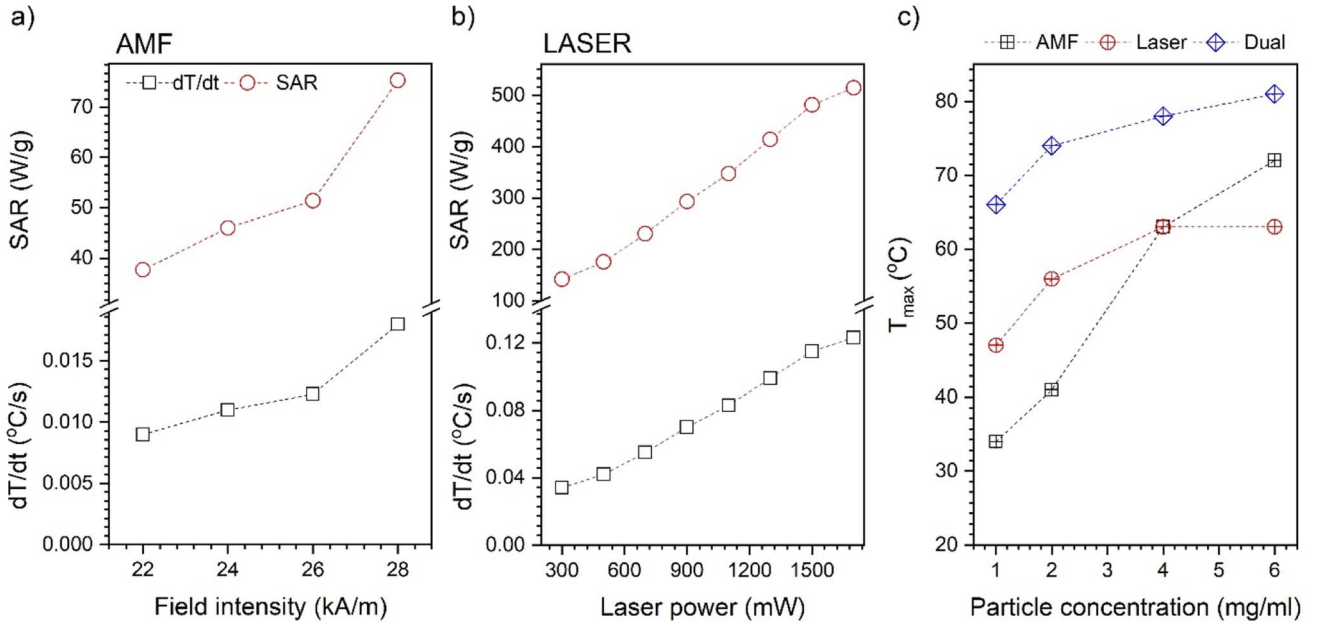

Fig. 8 Dependence of the magnetic field intensity (a) and laser power (b) on SAR and dT/dt values. Plot (c) shows nanoparticle concentration dependence on the T_{max} under different stimulation modes.

with a concentration of 1 mg ml^{-1} exclusively. As reference material for comparison of the heating efficacy of Fe_3O_4@-APTES–Ag structures, bare cubic MNPs colloid was taken. The heating curves for the optimization steps are presented in Fig. 6. As one can note, the best working set between all available field frequencies and intensities for AMF action was 302 kHz and 28 kA m^{-1} (compare Fig. 6a and b). Upon action of the 808 nm NIR light constant increase of the laser output power up to 1700 mW leads to a consecutive increase in the ΔT. Interestingly, during the comparison of Fe_3O_4@APTES–Ag structures with bare Fe_3O_4 nanocubes, we observed that there is only a slight ΔT difference for the best working AMF and NIR parameters applied. The effective concentration of magnetic material in the complex structure will be lower because of the presence of silica shell and silver particles. Another feature that could take place is that the silica shell and decorated silver particles can help reduce dipole–dipole magnetic interactions since their size accounts for the increase in distance between magnetic cores.[38] This type of interaction between particles has already been shown to have a detrimental effect on heat generation.[6] The heating mechanism induced by NIR radiation is not related to the heat losses generated by AMF. The temperature effect will depend on the absorption properties of the given material and the further dissipation of energy through non-radiative pathways.[9] As one can see, the response of the core–shell sample to the 808 nm irradiation is strikingly greater than that of AMF and extreme ΔT values can be achieved depending on the applied laser power (almost 50 °C). No saturation effect was observed within the laser power range studied, meaning that a further increase of this parameter will result in even higher ΔT.

Based on the behavior of the Fe_3O_4@APTES–Ag sample upon exposure to both stimulants, it was decided that the so-called dual-mode will be carried out to check if there will be any beneficial outcome that improves the heating efficiency. For dual-mode measurement, most optimal magnetic field parameters were applied, namely 302 kHz and 28 kA m^{-1}, while for NIR laser it was decided that we will limit the laser power to 900 mW to not overcome the AMF heat induction mechanism, and to significantly reduce the laser optical density (around 1 W cm^{-2}).

All recorded heating curves were presented in Fig. 7 in a way that allows the comparison of the AMF, laser, and dual modes separately. Furthermore, the effect of particle concentration was studied as well. The values of dT/dt that define the speed of the temperature increase, ΔT, and T_{max} were extracted and presented in Fig. 8. In general, dual-mode heat induction results in improvement of ΔT (Fig. 7) and the highest achievable T_{max} values (Fig. 8c). Separate AMF and NIR action gives in all cases a lower T_{max} than during dual exposure. The progressive increase of Fe_3O_4@APTES–Ag concentration increases T_{max} in an almost linear manner for AMF stimulation, which can be an indication of the absence of changes in particle state in suspensions.[39] What is worth noting, is that the above concentration of 4 mg ml^{-1} AMF heat induction starts to dominate over laser exposure leading to the higher T_{max} while at this concentration the saturation is already achieved for NIR action though the further increase of the nanoheaters does not change the T_{max} at all. The reason for that can be sought in the blocking of light penetration through the colloid due to the high number of NIR absorbers (critical concentration achieved) that are located at the proximal portion of dispersion. This fact can be supported by the data presented in Fig. 6c that showed a progressive temperature increase with laser power without achieving a saturation for the Fe_3O_4@APTES–Ag particles concentration of

Table 1 Specific absorption rate (SAR), dT/dt, ΔT, and T_{max} parameters of the Fe_3O_4 reference nanocubes and Fe_3O_4@APTES–Ag core–shell structures under contactless stimulation with AMF, laser, and synergic action. The corresponding magnetic field frequency was 302 kHz (optimal setting)

AMF				
Field intensity (kA m^{-1})	dT/dt (°C s^{-1})	ΔT	T_{max} (°C)	SAR (W g^{-1})
Fe_3O_4				
28	0.023	13.3	37.1	96.2
Fe_3O_4@APTES–Ag				
22	0.009	6.3	28.4	37.7
24	0.011	8.2	30.5	46.0
26	0.012	9.5	31.6	51.4
28	0.018	12.4	33.9	75.3
LASER				
Laser power (mW)	dT/dt (°C s^{-1})	ΔT	T_{max} (°C)	SAR (W g^{-1})
Fe_3O_4				
1700	0.138	48.6	74.5	579.6
Fe_3O_4@APTES–Ag				
300	0.034	9.6	34.2	142.3
500	0.042	16.6	41.9	175.8
700	0.055	21.6	46.7	230.2
900	0.070	26.8	50.4	292.9
1100	0.083	31.3	56.8	347.3
1300	0.099	37.5	62.6	414.3
1500	0.115	41.5	67.3	481.3
1700	0.123	46.4	71.9	514.7
DUAL				
AMF & laser parameters	dT/dt (°C s^{-1})	ΔT	T_{max} (°C)	SAR (W g^{-1})
Fe_3O_4@APTES–Ag 302 kHz, 28 kA m^{-1}, 900 mW	0.180	26.8	66.4	1031.9

Table 2 Fe_3O_4@APTES–Ag particle concentration dependence of dT/dt, ΔT, and T_{max} values extracted for different external stimulations

Concentration (mg ml^{-1})	dT/dt (°C/s^{-1})	ΔT	T_{max} (°C)
AMF 302 kHz 28 kA m^{-1}			
1	0.018	12.4	33.9
2	0.021	18.0	40.8
4	0.079	41.8	63.5
6	0.159	49.8	71.4
LASER 900 mW			
1	0.070	26.8	50.4
2	0.090	31.0	56.2
4	0.120	36.9	62.6
6	0.122	37.8	62.3
DUAL 302 kHz 28 kA m^{-1} 900 mW			
1	0.181	26.8	66.4
2	0.242	51.3	74.6
4	0.20	55.9	78.6
6	0.21	57.5	81.7

1 mg ml^{-1}. The saturation forced by the core–shell concentration was also noticeable for dual-mode energy conversion. Utilization of the laser light leads to the observed saturation regime that depends on the particle number due to the same reason mentioned. However, one can note that the heating efficiency during simultaneous action of AMF and NIR can be strongly enhanced and this augmentation has an almost cumulative character.

The specific absorption rate (SAR), being a measure of the heating performance, was calculated using the following formula:

$$\mathrm{SAR} = \frac{C}{m}\frac{\mathrm{d}T}{\mathrm{d}t}, \quad (1)$$

where C is the specific heat capacity of the medium (C_{H_2O} – 4.185 J g^{-1} °C^{-1}), m is the particle mass in dispersion (g), and dT/dt is the slope of the linear fit of the heating curve for the first tens of seconds. The results of the fitting (dT/dt) and calculations (SAR) with additional parameters (ΔT and T_{max}) were collected in Tables 1 and 2, while the chosen dependencies were presented in Fig. 8.

The SAR of the Fe_3O_4@APTES–Ag core–shell structures for the action of AMF was calculated for an optimized magnetic field frequency of 302 kHz as a function of field intensity and compared to bare Fe_3O_4 nanocubes. In general, the obtained values are below 100 W g^{-1} meaning that the heating efficiency of both samples is not impressively high. However, due to their size (above 60 nm), and the presence of strong interparticle interactions, SAR for bare Fe_3O_4 nanocubes (96 W g^{-1} calculated for the total Fe_3O_4 mass) is comparable with reports in the literature about similar objects.[6] It is worth mentioning that fabrication of the core–shell Fe_3O_4@APTES–Ag does not cause the loss of SAR. In our experiments, the values are very close to the uncovered cubes and we need to take into mind that within the same particle concentration the content of the iron will be lower than in a reference sample, though a drop in SAR was observed (75.3 instead of 96 W g^{-1}). Another reason can be sought in the presence of a silica insulating layer that can hinder heat dissipation, despite the thickness of about 10 nm. However, both samples at a particle concentration equal to 1 mg ml^{-1} cannot be heated above 40 °C and an increase of concentration (above 2 mg ml^{-1}) is necessary to achieve the biologically relevant temperature range when heated with AMF (see Table 2 and Fig. 7, 8c).

Significant heating with AMF can be achieved above 4 mg ml^{-1} of Fe_3O_4@APTES–Ag up to 71 °C. Upon analysis of the field intensity dependence of SAR and dT/dt (Fig. 8a), we found that both parameters change in a polynomial way (square). This trend should be expected by taking into account the Rosensweig work on the dissipation of power losses under AMF.[5] The heating effectiveness with NIR laser exposure is generally one order of magnitude greater in terms of SAR and dT/dt values,

pointing to a higher efficacy of the heating mechanism through photostimulation. For comparison, SAR for the AMF is 75.3 W g^{-1} and above 500 W g^{-1} for laser, while dT/dt changes from 0.018 °C s^{-1} to 0.123 °C s^{-1} when exposed to 808 nm wavelength at 1700 mW. As we can see, the SAR and dT/dt change linearly with laser output power as previously elucidated by others.[19] The maximum temperature that was achieved was 72 °C at 1700 mW. The concentration dependence for laser radiation was measured for the 900 mW (to limit LOD) and saturation was observed above 2 mg ml^{-1} meaning that in terms of NIR further increase of the nanoheaters number has no sense since no T_{max} is enhanced.

Interesting result has been achieved with dual-mode stimulation performed by using AMF with a field frequency of 302 kHz, 28 kA m^{-1} intensity, as well as 900 mW of laser output power. The greater augmentation of dT/dt was observed up to 0.2 °C s^{-1} while SAR was above 1000 W g^{-1} for the Fe_3O_4@-APTES–Ag concentration of 1 mg ml^{-1}. A further increase in the number of core–shell particles resulted in saturation similarly as for the laser mode alone. Comparison of the SAR values calculated for our heterostructures with the literature date is hard since one can find only one article authored by Das *et al.*[40] They reported SAR values for simultaneous action of AMF and laser light (442 nm instead of 808 nm and different LODs) of the order of 300 W g^{-1} (here 1000 W g^{-1}), but the field intensity was above 800 Oe (63 kA m^{-1}) instead of maximum of 28 kA m^{-1} in our case. We need to stress that they also used reverse heterostructures Ag@Fe_3O_4, so direct comparison is impossible.

3.3. Surface-enhanced Raman scattering on Fe_3O_4@APTES–Ag multipurpose platform

Verification of SERS augmentation on the prepared nanomaterials was performed with the rhodamine 6G standard (R6G). As one can observe, only with presence of the Fe_3O_4@APTES–Ag characteristic Raman bands of the R6G dye were revealed at characteristic positions 611, 773, 1188, 1311, 1362, 1421, 1506, 1573, 1655 cm^{-1}, respectively (see Fig. 9a and inset).[41,42] All other materials, including the R6G dye alone, did not generate any signal for 2.5 μM at 0.25 μW. Clearly, the presence of Ag metallic islands in Fe_3O_4@APTES–Ag promotes the SERS electromagnetic mechanism that results in a strong enhancement of the Raman signal that allows detection of the R6G analyte. The SERS sensitivity was tested using R6G standard solutions with the following concentrations 0.01, 0.05, 0.5, 1 and 2.5 μM (Fig. 9a). It should be noted that the R6G Raman bands can be detected down to 0.05 μM (50 nM) of the dye. Below that concentration no Raman modes were visible at 25 μW of laser power. The dependence of the 488 nm laser output power (25 μW–0.5 mW) on signal detectability was checked for the 0.5 μM R6G sample and shown in Fig. 9b. Approximately three-fold SERS signal improvement was observed meaning that the change in excitation power can be used for detection of lower R6G dye concentration, thus it can surpass the mention limit below 0.05 μM. Recently, it was shown that the excellent SERS probe was constructed based on purely Au snowflake NPs that is capable of detecting R6G at the level of 3 nM.[43,44] However, it is hard to estimate what laser power was used in the experiments, since no data was provided. At the same time, one has to remember that SERS probe sensitivity depends strongly on the source laser output power and can be also detrimental on the stability of measured analyte (generated heat can damage molecules).[45] Therefore, in the case of our Fe_3O_4@Ag heterostructures, we were able to detect the R6G at 50 nM and with the use of a low laser power that does not exceed 25 μW. As it was also shown by us, increase of the source power can enhance the signal intensity and as a consequence, increase the sensitivity of the probe significantly, as was presented by us in Fig. 9b. Another practical aspect can be found in the fact that the SERS

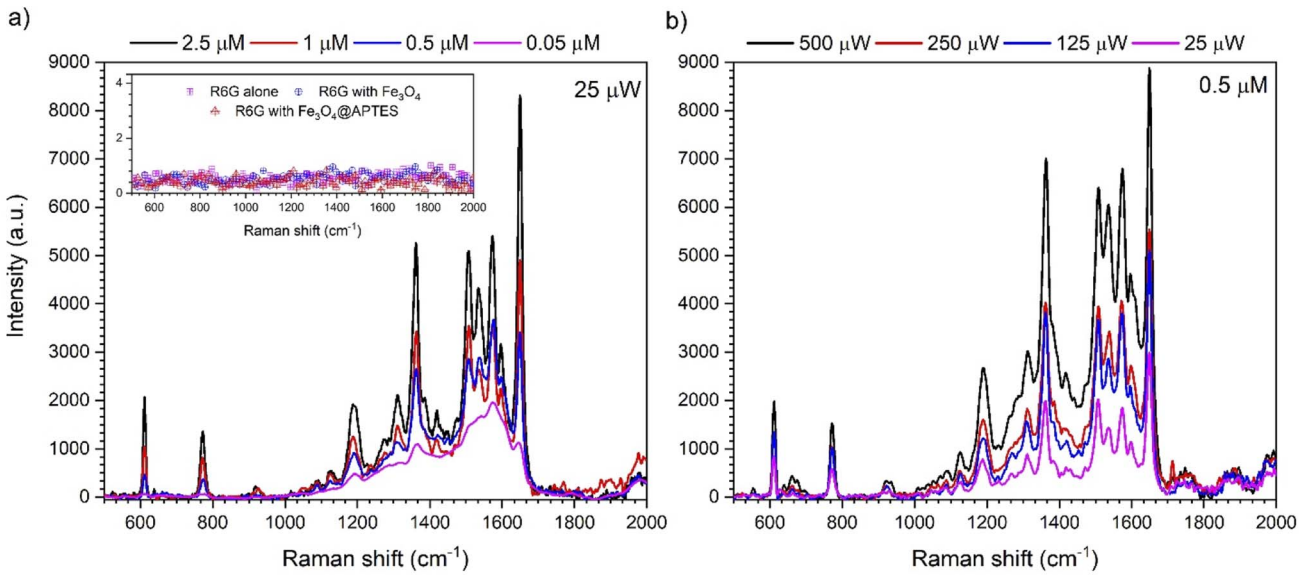

Fig. 9 SERS effect on Fe_3O_4@APTES–Ag heterostructures (a) as a function of R6G standard solution concentration recorded with 25 μW laser power (inset shows no signal recorded neither for R6G alone, R6G on Fe_3O_4 nor Fe_3O_4@APTES) as well as (b) as a function of the 488 nm laser power measured for 0.5 μM of R6G.

probe based on magnetic core heterostructures can be quite easily recovered and reused. Thus, we conclude that the proposed platform possesses sufficient sensitivity to be applied as a SERS probe.

3.4. Antibacterial activity of Fe_3O_4@APTES–Ag heterostructures

Fe_3O_4 particles are recognized in general as inert for bacteria. However, after silver-nanostructures decoration, they are likely to exhibit antibacterial activity. For this purpose, the minimum inhibitory concentration of the nanocubes was determined against four bacterial strains prevalent in nosocomial and medical devices-related infections. The results revealed, as expected, that bare Fe_3O_4 nanocubes did not show any antibacterial activity in concentrations up to 500 μg ml^{-1}. Fe_3O_4@APTES–Ag nanocubes were not effective against both tested Gram-positive strains as well as against *E. coli* (up to 50 μg ml^{-1}). However, they inhibited the growth of the *P. aeruginosa* strain at a concentration of 50 μg ml^{-1} (Table 3). This observation is particularly interesting because *P. aeruginosa* is a critically dangerous bacterial strain associated with nosocomial infections, causing morbidity and mortality in many patients and remarkably resistant to antibacterial agents, thus difficult to eradicate.[46] Its mechanism of resistance to antibacterial factors is based on outer membrane permeability, efflux systems, antibiotic-inactivating enzymes, resistance by mutations and acquisition of resistance genes, biofilm-mediated resistance, and formation of persister cells.[46] It was reported to cause approximately 10% of hospital infections.[47–49] For this reason, the World Health Organization (WHO) has recently listed carbapenem-resistant *P. aeruginosa* as one of three bacterial species in which there is a critical need for the development of new antibiotics to treat infections.[50] Therefore, the sensitivity of *P. aeruginosa* to Fe_3O_4@APTES–Ag nanocubes deserves particular interest and further studies, although the MIC value is relatively high (50 μg ml^{-1}). However, this is understandable in view of the low percentage of silver in the overall structure of the nanocubes.

Interestingly, Fe_3O_4@APTES (without silver) also showed notable activity against *S. aureus* and *S. epidermidis* strains (50 μg ml^{-1} and 25 μg ml^{-1}, respectively; Table 3). *S. aureus* is usually reported as the most common nosocomial infection-causing bacteria.[51,52] Whereas *S. epidermidis*, although being a natural skin colonizer, is nowadays regarded as the most frequent cause of nosocomial infections and indwelling medical device-associated infections, mainly due to its high ability to form biofilm on the surfaces of such devices.[52,53] The reason of the antibacterial activity of APTES-capped Fe_3O_4 nanocubes is intriguing. APTES contains amino groups which can bring benefits in increasing of antibacterial activity of Fe_3O_4 particles. It was earlier reported[54] that recombinant peptides with numerous amino acid residues showed antibacterial activity. Moreover, it was demonstrated that APTES-modified ZnO particles induced an antimicrobial effect, in particular against Gram-negative bacteria,[55] APTES modification of TiO_2 NPs enhanced the antibacterial efficiency against *Escherichia coli* under artificial solar light[56] and APTES-functionalized zeolite shows evidence of antibacterial activity against both Gram-positive and Gram-negative strains.[57] Thus, it seems that this phenomenon also deserves more attention in further studies because APTES-coating of nanostructures may form a platform for their further modifications, increasing their antimicrobial potential.

Table 3 Minimum inhibitory concentrations (MICs) of tested nanocubes against 4 reference bacterial strains: *Staphylococcus aureus* ATCC 25923 (*S.a.*), *Staphylococcus epidermidis* ATCC 12228 (*S.e.*), *Escherichia coli* ATCC 25922 (*E.c.*) and *Pseudomonas aeruginosa* ATCC 27953 (*P.a.*)

NPs		MIC (μg ml^{-1})			
Sample	Concentration range (μg ml^{-1})	*S.a.*	*S.e.*	*E.c.*	*P.a.*
Fe_3O_4	50–500	>500	>500	>500	>500
Fe_3O_4@APTES	1.562–50	50	25	>50	>50
Fe_3O_4@APTES–Ag	1.562–50	>50	>50	>50	50

4. Conclusions

The Fe_3O_4@APTES–Ag heterostructures were synthesized using a three-step process involving the synthesis of the magnetite nanocube core material, surface coverage with a thin silica shell, and chemisorption of Ag^+ cations and their subsequent reduction resulting in the formation of silver metallic islands. The estimated size of the multipurpose composite was around 94.5 nm, while Ag silver particles were of 8.5 nm interconnected with the Fe_3O_4 surface through a silica shell with an average thickness of 12.8 nm. The effectiveness of heterostructure fabrication was evidenced by the TEM imaging and FTIR-ATR spectroscopy. The silica shell and silver particles are clearly distinguishable, as well as FTIR gave an indication of the Fe_3O_4 surface coverage and Ag attachment that manifested in the shift of the characteristic vibration bands and the appearance of new features.

The multifunctionality of Ag-decorated Fe_3O_4 nanoparticles was manifested in the ability to generate significant temperature effects under the action of AMF and NIR radiation, to use it as a SERS probe and antimicrobial activity. In the case of heat induction, Fe_3O_4 heterostructures showed exceptional responsiveness to synergic action of AMF and NIR (808 nm laser light) that resulted in a high SAR value of 1000 W g^{-1}. The laser-induced energy conversion was more effective than AMF stimulation, with one order of magnitude higher dT/dt in the first case. It was shown that even the AMF-based mechanism is not that efficient; the temperature effect can be enhanced by increasing the concentration of nanoheaters, leading to a T_{max} of 71 °C. Increase of the same particle concentration during laser exposure leads to saturation above 2 mg ml^{-1}, and the same behavior was observed for dual mode stimulation.

The verification of the ability of Fe_3O_4@APTES–Ag to enhance the Raman signal of the R6G molecule was confirmed. The detection limit of R6G can be augmented by modulating the

incident laser power and can be increased below 0.01 μM of the dye.

The antimicrobial activity of the heterostructures was tested against four bacterial strains, *Staphylococcus aureus* ATCC 25923, *Staphylococcus epidermidis* ATCC 12228, *Escherichia coli* ATCC 25922 and *Pseudomonas aeruginosa* ATCC 27953. The Fe_3O_4@APTES–Ag showed the highest activity for inhibition of *P. aeruginosa* at 50 μg ml^{-1}. This is a very interesting effect from the application point of view, since *P. aeruginosa* is an extremely dangerous bacteria that causes high mortality in patients and is very resistant to antibacterial agents.

Author contributions

M. K.-G., D.S. and A.T. synthesis of particles, heterostructures, and their characterization, M. K.-G., D. S. energy conversion measurements, R. P. and M. K.-G. data analysis and figures preparation, A. D. particle imaging, and element mapping, A. M. and A. B. antimicrobial activity tests, data analysis, R. W.-N. SERS experiments and data analysis, R. P., A. T., M. K.-G., A. T, D. S., A. D., A. M., A. B., R. W.-N., writing manuscript, editing and corrections. R. P., M. K.-G., A. B. idea, methodology, conceptualization. All authors read the manuscript and agreed with its content.

Conflicts of interest

There are no conflicts to declare.

Acknowledgements

Financial support of the National Science Centre, Poland in course of realization of Project no. UMO-2017/25/B/ST5/00497 is gratefully acknowledged. Antibacterial activity studies were supported by the Ministry of Education and Science in Poland within the statutory activity of the Medical University of Lublin (DS6/2022). The authors would like to thank M.Sc. Eng. Patrycja Kłoda-Biskup for technical assistance.

References

1 R. Hergt, S. Dutz, R. Müller and M. Zeisberger, Magnetic Particle Hyperthermia: Nanoparticle Magnetism and Materials Development for Cancer Therapy, *J. Phys.: Condens. Matter*, 2006, **18**, S2919–S2934, DOI: 10.1088/0953-8984/18/38/S26.

2 S. Dutz and R. Hergt, Magnetic Nanoparticle Heating and Heat Transfer on a Microscale: Basic Principles, Realities and Physical Limitations of Hyperthermia for Tumour Therapy, *Int. J. Hyperthermia*, 2013, **29**, 790–800, DOI: 10.3109/02656736.2013.822993.

3 L. Wu, A. Mendoza-Garcia, Q. Li and S. Sun, Organic Phase Syntheses of Magnetic Nanoparticles and Their Applications, *Chem. Rev.*, 2016, **116**, 10473–10512, DOI: 10.1021/acs.chemrev.5b00687.

4 M. Banobre-Lopez, Y. Pineiro-Redondo, M. Sandri, A. Tampieri, R. De Santis, V. A. Dediu and J. Rivas, Hyperthermia Induced in Magnetic Scaffolds for Bone Tissue Engineering, *IEEE Trans. Magn.*, 2014, **50**, 5400507, DOI: 10.1109/TMAG.2014.2327245.

5 R. E. Rosensweig, Heating Magnetic Fluid with Alternating Magnetic Field, *J. Magn. Magn. Mater.*, 2002, **252**, 370–374, DOI: 10.1016/S0022-5347(17)32321-2.

6 H. Gavilán, S. K. Avugadda, T. Fernández-Cabada, N. Soni, M. Cassani, B. T. Mai, R. Chantrell and T. Pellegrino, Magnetic Nanoparticles and Clusters for Magnetic Hyperthermia: Optimizing Their Heat Performance and Developing Combinatorial Therapies to Tackle Cancer, *Chem. Soc. Rev.*, 2021, **50**(20), 11614–11667, DOI: 10.1039/d1cs00427a.

7 A. K. A. Silva, A. Espinosa, J. Kolosnjaj-Tabi, C. Wilhelm and F. Gazeau, Medical Applications of Iron Oxide Nanoparticles, in *Iron Oxides: From Nature to Applications*, ed. D. Faivre, Wiley-VCH Verlag GmbH & Co. KGaA, 2016, pp. 425–471, DOI: 10.1002/9783527691395.ch18.

8 A. G. Roca, L. Gutiérrez, H. Gavilán, M. E. Fortes Brollo, S. Veintemillas-Verdaguer and M. P. Morales, Design Strategies for Shape-Controlled Magnetic Iron Oxide Nanoparticles, *Adv. Drug Delivery Rev.*, 2019, **138**, 68–104, DOI: 10.1016/j.addr.2018.12.008.

9 D. Jaque, L. Martínez Maestro, B. del Rosal, P. Haro-Gonzalez, A. Benayas, J. L. Plaza, E. Martín Rodríguez and J. García Solé, Nanoparticles for Photothermal Therapies, *Nanoscale*, 2014, **6**, 9494–9530, DOI: 10.1039/c4nr00708e.

10 L. M. Maestro, P. Haro-González, B. del Rosal, J. Ramiro, a J. Caamaño, E. Carrasco, A. Juarranz, F. Sanz-Rodríguez, J. G. Solé and D. Jaque, Heating Efficiency of Multi-Walled Carbon Nanotubes in the First and Second Biological Windows, *Nanoscale*, 2013, **5**(17), 7882–7889, DOI: 10.1039/c3nr01398g.

11 S. Link and M. A. El-Sayed, Shape and Size Dependence of Radiative, Non-Radiative and Photothermal Properties of Gold Nanocrystals, *Int. Rev. Phys. Chem.*, 2000, **19**, 409–453, DOI: 10.1080/01442350050034180.

12 T. N. Lambert, N. L. Andrews, H. Gerung, T. J. Boyle, J. M. Oliver, B. S. Wilson and S. M. Han, Water-Soluble Germanium(0) Nanocrystals: Cell Recognition and near-Infrared Photothermal Conversion Properties, *Small*, 2007, **3**(4), 691–699, DOI: 10.1002/smll.200600529.

13 X. H. Huang, I. H. El-Sayed, W. Qian and M. a. El-Sayed, Cancer Cell Imaging and Photothermal Therapy in the Near-Infrared Region by Using Gold Nanorods, *J. Am. Chem. Soc.*, 2006, **128**(6), 2115–2120, DOI: 10.1021/ja057254a.

14 S. Shen, F. Kong, X. Guo, L. Wu, H. Shen, M. Xie, X. Wang, Y. Jin and Y. Ge, CMCTS Stabilized Fe3O4 Particles with Extremely Low Toxicity as Highly Efficient Near-Infrared Photothermal Agents for in Vivo Tumor Ablation, *Nanoscale*, 2013, **5**(17), 8056–8066, DOI: 10.1039/c3nr01447a.

15 S. Shen, S. Wang, R. Zheng, X. Zhu, X. Jiang, D. Fu and W. Yang, Magnetic Nanoparticle Clusters for Photothermal Therapy with Near-Infrared Irradiation, *Biomaterials*, 2015, **39**, 67–74, DOI: 10.1016/j.biomaterials.2014.10.064.

16 M. Chu, Y. Shao, J. Peng, X. Dai, H. Li, Q. Wu and D. Shi, Near-Infrared Laser Light Mediated Cancer Therapy by Photothermal Effect of Fe3O4 Magnetic Nanoparticles, *Biomaterials*, 2013, **34**, 4078–4088, DOI: 10.1016/j.biomaterials.2013.01.086.

17 J. Estelrich and M. Antònia Busquets, Iron Oxide Nanoparticles in Photothermal Therapy, *Molecules*, 2018, **23**, 1567, DOI: 10.3390/molecules23071567.

18 H. Chen, J. Burnett, F. Zhang, J. Zhang, H. Paholak and D. Sun, Highly Crystallized Iron Oxide Nanoparticles as Effective and Biodegradable Mediators for Photothermal Cancer Therapy, *J. Mater. Chem. B*, 2014, **2**(7), 757–765, DOI: 10.1039/c3tb21338b.

19 H. Rodríguez-Rodríguez, G. Salas and J. R. Arias-Gonzalez, Heat Generation in Single Magnetic Nanoparticles under Near-Infrared Irradiation, *ACS Appl. Mater. Interfaces*, 2020, 2182–2187, DOI: 10.1021/acs.jpclett.0c00143.

20 A. Espinosa, R. Di Corato, J. Kolosnjaj-Tabi, P. Flaud, T. Pellegrino and C. Wilhelm, Duality of Iron Oxide Nanoparticles in Cancer Therapy: Amplification of Heating Efficiency by Magnetic Hyperthermia and Photothermal Bimodal Treatment, *ACS Nano*, 2016, **10**, 2436–2446, DOI: 10.1021/acsnano.5b07249.

21 A. Espinosa, J. Kolosnjaj-Tabi, A. Abou-Hassan, A. Plan Sangnier, A. Curcio, A. K. A. Silva, R. Di Corato, S. Neveu, T. Pellegrino, L. M. Liz-Marzán and C. Wilhelm, Magnetic (Hyper)Thermia or Photothermia? Progressive Comparison of Iron Oxide and Gold Nanoparticles Heating in Water, in Cells, and In Vivo, *Adv. Funct. Mater.*, 2018, **28**(37), 1–16, DOI: 10.1002/adfm.201803660.

22 D. H. Ortgies, F. J. Teran, U. Rocha, L. de la Cueva, G. Salas, D. Cabrera, A. S. Vanetsev, M. Rähn, V. Sammelselg, Y. V. Orlovskii and D. Jaque, Optomagnetic Nanoplatforms for In Situ Controlled Hyperthermia, *Adv. Funct. Mater.*, 2018, **28**, 1–11, DOI: 10.1002/adfm.201704434.

23 M. Kulpa-Greszta, R. Pązik, P. Kłoda, A. Tomaszewska, E. Zachanowicz, K. Pałka, G. Ginalska and A. Belcarz, Efficient Non-Contact Heat Generation on Flexible, Ternary Hydroxyapatite/Curdlan/Nanomagnetite Hybrids for Temperature Controlled Processes, *Mater. Sci. Eng., C*, 2021, **118**, 111360, DOI: 10.1016/j.msec.2020.111360.

24 M. A. Antoniak, R. Pązik, U. Bazylińska, K. Wiwatowski, A. Tomaszewska, M. Kulpa-Greszta, J. Adamczyk-Grochala, M. Wnuk, S. Maćkowski, A. Lewińska and M. Nyk, Multimodal Polymer Encapsulated CdSe/Fe3O4 Nanoplatform with Improved Biocompatibility for Two-Photon and Temperature Stimulated Bioapplications, *Mater. Sci. Eng., C*, 2021, **127**, 112224, DOI: 10.1016/j.msec.2021.112224.

25 R. Pązik, A. Lewińska, J. Adamczyk-Grochala, M. Kulpa-Greszta, P. Kłoda, A. Tomaszewska, A. Dziedzic, G. Litwienienko, M. Noga, D. Sikora and M. Wnuk, Energy Conversion and Biocompatibility of Surface Functionalized Magnetite Nanoparticles with Phosphonic Moieties, *J. Phys. Chem. B*, 2020, **124**, 4931–4948, DOI: 10.1021/acs.jpcb.0c02808.

26 S. A. Sapareto and W. C. Dewey, Thermal Dose Determination in Cancer Therapy, *Int. J. Radiat. Oncol., Biol., Phys.*, 1984, **10**, 787–800, DOI: 10.1016/0360-3016(84)90379-1.

27 C. Wang, Z. Rong, J. Wang, N. Jiang, Y. Pang, R. Xiao and S. Wang, Seed-Mediated Synthesis of High-Performance Silver-Coated Magnetic Nanoparticles and Their Use as Effective SERS Substrates, *Colloids Surf., A*, 2016, **506**, 393–401, DOI: 10.1016/j.colsurfa.2016.05.103.

28 D. Song, R. Yang, C. Wang, R. Xiao and F. Long, Reusable Nanosilver-Coated Magnetic Particles for Ultrasensitive SERS-Based Detection of Malachite Green in Water Samples, *Sci. Rep.*, 2016, **6**, 1–9, DOI: 10.1038/srep22870.

29 K. S. Shin, Y. K. Cho, J. Y. Choi and K. Kim, Facile Synthesis of Silver-Deposited Silanized Magnetite Nanoparticles and Their Application for Catalytic Reduction of Nitrophenols, *Appl. Catal., A*, 2012, **413–414**, 170–175, DOI: 10.1016/j.apcata.2011.11.006.

30 H. M. A. Sharif, A. Mahmood, H. Y. Cheng, R. Djellabi, J. Ali, W. L. Jiang, S. S. Wang, M. R. Haider, N. Mahmood and A. J. Wang, Fe3O4 Nanoparticles Coated with EDTA and Ag Nanoparticles for the Catalytic Reduction of Organic Dyes from Wastewater, *ACS Appl. Nano Mater.*, 2019, **2**, 5310–5319, DOI: 10.1021/acsanm.9b01250.

31 M. Abbas, S. R. Torati and C. G. Kim, A Novel Approach for the Synthesis of Ultrathin Silica-Coated Iron Oxide Nanocubes Decorated with Silver Nanodots (Fe3O4/SiO2/Ag) and Their Superior Catalytic Reduction of 4-Nitroaniline, *Nanoscale*, 2015, **7**(28), 12192–12204, DOI: 10.1039/c5nr02680f.

32 X. Zhang, H. Niu, J. Yan and Y. Cai, Immobilizing Silver Nanoparticles onto the Surface of Magnetic Silica Composite to Prepare Magnetic Disinfectant with Enhanced Stability and Antibacterial Activity, *Colloids Surf., A*, 2011, **375**(1–3), 186–192, DOI: 10.1016/j.colsurfa.2010.12.009.

33 D. Kim, N. Lee, M. Park, B. H. Kim, K. An and T. Hyeon, Synthesis of Uniform Ferrimagnetic Magnetite Nanocubes - Journal of the American Chemical Society (ACS Publications), *J. Am. Chem. Soc.*, 2009, **131**, 454–455, DOI: 10.1021/ja8086906.

34 P. S. Goh, T. W. Wong, J. W. Lim, A. F. Ismail and N. Hilal, Innovative and Sustainable Membrane Technology for Wastewater Treatment and Desalination Application, in *Innovation Strategies in Environmental Science*, ed. C. M. Galanakis, Elsevier Inc., 2019, pp. 291–319, DOI: 10.1016/B978-0-12-817382-4.00009-5.

35 L. Qiao, Z. Fu, J. Li, J. Ghosen, M. Zeng, J. Stebbins, P. N. Prasad and M. T. Swihart, Standardizing Size- and Shape-Controlled Synthesis of Monodisperse Magnetite (Fe3O4) Nanocrystals by Identifying and Exploiting Effects of Organic Impurities, *ACS Nano*, 2017, **11**, 6370–6381, DOI: 10.1021/acsnano.7b02752.

36 D. W. Wang, X. M. Zhu, S. F. Lee, H. M. Chan, H. W. Li, S. K. Kong, J. C. Yu, C. H. K. Cheng, Y. X. J. Wang and K. C. F. Leung, Folate-Conjugated Fe3O4@SiO2@gold Nanorods@mesoporous SiO2 Hybrid Nanomaterial: A

Theranostic Agent for Magnetic Resonance Imaging and Photothermal Therapy, *J. Mater. Chem. B*, 2013, **1**(23), 2934–2942, DOI: **10.1039/c3tb20090f**.

37 J. Xu, C. Ju, J. Sheng, F. Wang, Q. Zhang, G. Sun and M. Sun, Synthesis and Characterization of Magnetic Nanoparticles and Its Application in Lipase Immobilization, *Bull. Korean Chem. Soc.*, 2013, **34**, 2408–2412, DOI: **10.5012/bkcs.2013.34.8.2408**.

38 A. Morel, S. I. Nikitenko, K. Gionnet, A. Wattiaux, J. Lai-kee-him, C. Labrugere, B. Chevalier, G. Deleris, C. Petibois, A. Brisson, M. Simonoff, I. Bordeaux, L. H. Vigneau and A. Faculte, Sonochemical Approach to the Synthesis, *ACS Nano*, 2008, **2**, 847–856.

39 M. Zeinoun, J. Domingo-Diez, M. Rodriguez-Garcia, O. Garcia, M. Vasic, M. Ramos and J. J. S. Olmedo, Enhancing Magnetic Hyperthermia Nanoparticle Heating Efficiency with Non-Sinusoidal Alternating Magnetic Field Waveforms, *Nanomaterials*, 2021, **11**, 3240, DOI: **10.3390/nano11123240**.

40 R. Das, N. Rinaldi-Montes, J. Alonso, Z. Amghouz, E. Garaio, J. A. García, P. Gorria, J. A. Blanco, M. H. Phan and H. Srikanth, Boosted Hyperthermia Therapy by Combined AC Magnetic and Photothermal Exposures in Ag/Fe3O4 Nanoflowers, *ACS Appl. Mater. Interfaces*, 2016, **8**, 25162–25169, DOI: **10.1021/acsami.6b09942**.

41 P. Hildebrandt and M. Stockhurger, Surface-Enhanced Resonance Raman Spectroscopy of Rhodamine 6G Adsorbed on Colloidal Silver, *J. Phys. Chem.*, 1984, **88**, 5935–5944, DOI: **10.1021/j150668a038**.

42 C. Wu, E. Chen and J. Wei, Surface Enhanced Raman Spectroscopy of Rhodamine 6G on Agglomerates of Different-Sized Silver Truncated Nanotriangles, *Colloids Surf., A*, 2016, **506**, 450–456, DOI: **10.1016/j.colsurfa.2016.07.020**.

43 H. Zhou, X. Li, L. Wang, Y. Liang, A. Jialading, Z. Wang and J. Zhang, Application of SERS Quantitative Analysis Method in Food Safety Detection, *Rev. Anal. Chem.*, 2021, **40**, 173–186, DOI: **10.1515/revac-2021-0132**.

44 D. Huang, J. Zhao, M. Wang and S. Zhu, Snowflake-like Gold Nanoparticles as SERS Substrates for the Sensitive Detection of Organophosphorus Pesticide Residues, *Food Control*, 2020, **108**, 106835, DOI: **10.1016/j.foodcont.2019.106835**.

45 Z. D. Schultz, Not Too Hot: The Importance of Optimizing Laser Power for Surface-Enhanced Raman Spectroscopy (SERS) Measurements, *Spectrsocopy*, 2021, **36**, 18–20.

46 Z. Pang, R. Raudonis, B. R. Glick, T. J. Lin and Z. Cheng, Antibiotic Resistance in Pseudomonas Aeruginosa: Mechanisms and Alternative Therapeutic Strategies, *Biotechnol. Adv.*, 2019, **37**, 177–192, DOI: **10.1016/j.biotechadv.2018.11.013**.

47 D. Cardo, T. Horan, M. Andrus, M. Dembinski, J. Edwards, G. Peavy, J. Tolson and D. Wagner, *National Nosocomial Infections Surveillance (NNIS) System Report, Data Summary from January 1992 through June 2004, Issued October 2004*, 2004, vol. 32, DOI: **10.1016/j.ajic.2004.10.001**.

48 R. Recio, M. Mancheno, E. Viedma, J. Villa, M. A. Orellana, J. Lora-Tamayo and F. Chaves, Predictors of Mortality in Bloodstream Infections Caused by Pseudomonas Aeruginosa and Impact of Antimicrobial, *Antimicrob. Agents Chemother.*, 2020, **64**, e01759-19, DOI: **10.1128/aac.01759-19**.

49 H. S. Sader, M. Castanheira, L. R. Duncan and R. K. Flamm, Antimicrobial Susceptibility of Enterobacteriaceae and Pseudomonas Aeruginosa Isolates from United States Medical Centers Stratified by Infection Type: Results from the International Network for Optimal Resistance Monitoring (INFORM) Surveillance Program, *Diagn. Microbiol. Infect. Dis.*, 2018, **92**, 69–74, DOI: **10.1016/j.diagmicrobio.2018.04.012**.

50 E. Tacconelli, E. Carrara, A. Savoldi, S. Harbarth, M. Mendelson, D. L. Monnet, C. Pulcini, G. Kahlmeter, J. Kluytmans, Y. Carmeli, M. Ouellette, K. Outterson, J. Patel, M. Cavaleri, E. M. Cox, C. R. Houchens, M. L. Grayson, P. Hansen, N. Singh, U. Theuretzbacher, N. Magrini, A. O. Aboderin, S. S. Al-Abri, N. Awang Jalil, N. Benzonana, S. Bhattacharya, A. J. Brink, F. R. Burkert, O. Cars, G. Cornaglia, O. J. Dyar, A. W. Friedrich, A. C. Gales, S. Gandra, C. G. Giske, D. A. Goff, H. Goossens, T. Gottlieb, M. Guzman Blanco, W. Hryniewicz, D. Kattula, T. Jinks, S. S. Kanj, L. Kerr, M. P. Kieny, Y. S. Kim, R. S. Kozlov, J. Labarca, R. Laxminarayan, K. Leder, L. Leibovici, G. Levy-Hara, J. Littman, S. Malhotra-Kumar, V. Manchanda, L. Moja, B. Ndoye, A. Pan, D. L. Paterson, M. Paul, H. Qiu, P. Ramon-Pardo, J. Rodríguez-Baño, M. Sanguinetti, S. Sengupta, M. Sharland, M. Si-Mehand, L. L. Silver, W. Song, M. Steinbakk, J. Thomsen, G. E. Thwaites, J. W. van der Meer, N. Van Kinh, S. Vega, M. V. Villegas, A. Wechsler-Fördös, H. F. L. Wertheim, E. Wesangula, N. Woodford, F. O. Yilmaz and A. Zorzet, Discovery, Research, and Development of New Antibiotics: The WHO Priority List of Antibiotic-Resistant Bacteria and Tuberculosis, *Lancet Infect. Dis.*, 2018, **18**, 318–327, DOI: **10.1016/S1473-3099(17)30753-3**.

51 T. Ananda, A. Modi, I. Chakraborty, V. Managuli, C. Mukhopadhyay and N. Mazumder, Nosocomial Infections and Role of Nanotechnology, *Bioengineering*, 2022, **9**, 51, DOI: **10.3390/bioengineering9020051**.

52 N. A. Nimer, Nosocomial Infection and Antibiotic-Resistant Threat in the Middle East, *Infect. Drug Resist.*, 2022, **15**, 631–639, DOI: **10.2147/IDR.S351755**.

53 K. L. Rogers, P. D. Fey and M. E. Rupp, Coagulase-Negative Staphylococcal Infections, *Infect. Dis. Clin.*, 2009, **23**, 73–98, DOI: **10.1016/j.idc.2008.10.001**.

54 M. Stetsenko, T. Margitych, S. Kryvyi, L. Maksimenko, A. Hassan, S. Filonenko, B. Li, J. Qu, E. Scheer and S. Snegir, Gold Nanoparticle Self-Aggregation on Surface with 1,6-Hexanedithiol Functionalization, *Nanomaterials*, 2020, **10**, 512, DOI: **10.3390/nano10030512**.

55 S. C. Esparza-González, S. Sánchez-Valdés, S. N. Ramírez-Barrón, M. J. Loera-Arias, J. Bernal, H. I. Meléndez-Ortiz and R. Betancourt-Galindo, Effects of Different Surface Modifying Agents on the Cytotoxic and Antimicrobial Properties of ZnO Nanoparticles, *Toxicol. In Vitro*, 2016, **37**, 134–141, DOI: **10.1016/j.tiv.2016.09.020**.

56 P. Rokicka-Konieczna, A. Wanag, A. Sienkiewicz, E. Kusiak-Nejman and A. W. Morawski, Antibacterial Effect of TiO2 Nanoparticles Modified with APTES, *Catal. Commun.*, 2020, **134**, 105862, DOI: 10.1016/j.catcom.2019.105862.

57 S. A. Mohd Hanim, N. A. N. N. Malek, Z. Ibrahim, M. Mad Salim, N. I. Ramli, N. S. Sarah and M. A. Azam, Antibacterial Activity of Amine-Functionalized Zeolite NaY against *Staphylococcus Aureus* ATCC6538 and *Escherichia Coli* ATCC11229, *Appl. Mech. Mater.*, 2015, **761**, 402–406, DOI: 10.4028/www.scientific.net/amm.761.402.